Journal of Biomechanics 94 (2019) 88–98

Contents lists available at ScienceDirect

Journal of Biomechanics

journal homepage: www.elsevier.com/locate/jbiomech
www.JBiomech.com

Computational analysis of a flapping uvula on aerodynamics and pharyngeal wall collapsibility in sleep apnea

Junshi Wang [a], Jinxiang Xi [b,*], Pan Han [a], Niphattha Wongwiset [a], John Pontius [b], Haibo Dong [a,*]

[a] Department of Mechanical and Aerospace Engineering, University of Virginia, Charlottesville, VA, USA
[b] Department of Biomedical Engineering, California Baptist University, Riverside, CA, USA

ARTICLE INFO

Article history:
Accepted 14 July 2019

Keywords:
Sleep apnea
Flapping uvula
Pharyngeal wall collapse
Immersed boundary method (IBM)
Direct numerical simulation (DNS)

ABSTRACT

Studying the airflows and the resultant aerodynamic pressure/force in the pharyngeal airway is critical for understanding the pathophysiology of snoring and sleep apnea. In this work, an experiment-driven computational study was conducted to examine the aerodynamics in human pharyngeal airway. An anatomically accurate pharynx model associated with different uvula kinematics was reconstructed from human magnetic resonance image (MRI) and high-speed photography. An immersed-boundary-method (IBM)-based direct numerical simulation (DNS) flow solver was adopted to simulate the corresponding unsteady flows in all their complexity. Analyses were performed on vortex dynamics and pressure fluctuations in the pharyngeal airway and force oscillations on the pharyngeal wall under the influence of varying airway obstructions, uvula flapping mode, and uvula flapping frequencies. It was found the vortex formation, aerodynamic pressure, and pharyngeal wall force were significantly affected by the width of the pharyngeal airway. By contrast, the influences from the uvula flapping mode were insignificant when other parameters were similar. Fast Fourier transformation (FFT) and continuous wavelet transform (CWT) analysis of the pressure time history revealed the existence of higher order harmonics of base frequency with significant pressure amplitudes and energy intensities. It was also found the airway pressure and pharyngeal wall force oscillate more dramatically at higher uvula flapping frequencies, which tends to promote the collapse of pharyngeal wall and initiates sleep apnea.

1. Introduction

Obstructive sleep apnea (OSA) is a common breathing disorder during sleep (Young et al., 1993) associated with different levels of pharyngeal airway constriction and mostly loud snoring sound (Kavcic et al., 2013). The collapse of pharyngeal wall is the direct cause of the significantly reduced or completely ceased airflow through the upper airway of OSA patients. It is commonly believed that the collapsibility of the pharyngeal wall is subject to the interplay between external mechanical loads and subsequent neuromuscular responses (Patil et al., 2007). The fact that narrowed airways were found in patients with OSA suggests anatomically contracted airway could further increase the collapsibility of the pharyngeal wall (Arens et al., 2003) or soft palate (Liu et al., 2018a, 2019).

Besides the aforementioned mechanical/neuromuscular and anatomical causes, the flow-induced aerodynamic loads in human upper airway have been proven to be an important factor affecting snoring and OSA by extensive experimental (Ayappa and Rapoport, 2003) and computational fluid dynamics (CFD) studies (Mihaescu et al., 2011; Pirnar et al., 2015). Though Bernoulli's principle was found to be the major cause of reduced aerodynamic pressure in the pharynx (Fajdiga, 2005), enriched flow physics other than laminar flow happens in the processes of snoring and OSA, suggesting more complex pathological mechanisms driven by aerodynamics. Specifically, flow separation and recirculation can happen due to the irregular shape of human airway, even at its static condition, causing secondary and highly turbulent flows. CFD Studies have shown such unsteady flows in static airway models with significant vortical structures and pressure fluctuations (Mihaescu et al., 2011; Wang and Elghobashi, 2014; Xi et al., 2018a; Zhang and Kleinstreuer, 2011).

Moreover, fluid structure interaction (FSI) between airflows and vibrating airway structures, such as soft palate, tongue base, and uvula, could further increase the unsteadiness and complexity of the flow environment. Studies using FSI have found substantial

* Corresponding authors at: Department of Mechanical and Aerospace Engineering, University of Virginia, 122 Engineers Way, Charlottesville, VA 22904, USA (H. Dong). Department of Biomedical Engineering California Baptist University, 8432 Magnolia Avenue, Riverside, CA 92504, USA (J. Xi).
E-mail addresses: jxi@calbaptist.edu (J. Xi), haibo.dong@virginia.edu (H. Dong).

https://doi.org/10.1016/j.jbiomech.2019.07.014
0021-9290/

deformation at tongue base and soft palate (Huang et al., 2005; Liu et al., 2018b; Liu et al., 2007; Sun et al., 2007; Wang et al., 2012; Zhu et al., 2012), as well as airway collapse at the pharyngeal wall (Henrik Strand Moxness et al., 2018; Huang et al., 2013; Pirnar et al., 2015; Zhao et al., 2013).

However, the aerodynamic role of uvula was neglected or might be significantly underestimated in the aforementioned studies. Uvula is a hanging structure in the back of the throat. Pronounced uvula vibrations happen during snoring. The anatomical nature that the uvula is located in the upstream (during inhalation) of the pharynx indicates potential aerodynamic effect of uvula oscillations on the downstream airflows and consequent pressure loads on the pharyngeal wall. However, few experimental data on uvula kinematics during snoring can be found, and limited CFD studies have involved a dynamic uvula. Though the FSI study on soft palate has shown a promising sign of uvular influence on airflows (Pirnar et al., 2015; Sun et al., 2007; Zhu et al., 2012), whether uvula oscillations will increase the intensity of snoring sound and the collapsibility of the pharyngeal wall remains elusive.

The turbulent nature of airflows in snoring and OSA has stimulated the development of CFD algorithms to better resolve the flow details. Though studies using Reynolds-averaged Navier-Stokes (RANS) with turbulence models can capture major unsteady flow features(Liu et al., 2018b; Mylavarapu et al., 2009; Pirnar et al., 2015), large eddy simulation (LES) can better resolve the turbulent vortical structures (Powell et al., 2011; Xi et al., 2018b) and pressure fluctuations (Mihaescu et al., 2011). As the gold standard in numerical simulations, direct numerical simulation (DNS) can resolve the flow to the dissipative scale. Applications include simple geometries (Lin et al., 2007; Varghese et al., 2007) and static models (Li et al., 2017; Wang and Elghobashi, 2014).

The present study aims to quantitatively characterize the influences of uvula oscillation on airflows and aerodynamic pressure/force behaviors in an image-based airway geometry, which is the first to conduct DNS analysis on a dynamic uvula. Key variables, including the airway constriction, uvula flapping mode, and the flapping frequency of the uvula, are investigated. There are four specific aims: (1) developing a computational upper airway model with a flapping uvula, (2) characterizing the effects of uvular oscillations and airway narrowing on vortex dynamics and pressure fluctuations, (3) conducting spectrum analysis of the pressure signals including fast Fourier transformation (FFT) and continuous wavelet transform (CWT), and (4) examining the pressure and force behaviors on the pharyngeal wall for its collapsibility assessment. Two uvula flapping mode with various flapping frequencies in normal and constricted upper airway models, respectively, were considered in this study.

2. Methods

2.1. Computational model of upper airway with a flapping uvula

The computational model adopted in this study, as shown in Fig. 1a, contains the pharynx part of the human airway and the uvula. The morphology of the pharynx model was directly reconstructed from the human magnetic resonance image (MRI) data (Xi and Longest, 2008; Xi et al., 2014), and the uvula motion based on MRI data and high-speed photography of three subjects (Fig. 1c) was then added to the pharynx model.

Due to technical limitations, the dynamic MRI (Fig. 1b) was taken at a low frequency of 12 frames per second, which is insufficient to resolve the detailed kinematics of an oscillating uvula. To further investigate the kinematics of uvula, its motion during simulated snoring of three subjects (males, age: 25–27 years, BMI: 23.0–26.6) was recorded using a high-speed camera (Photron FASTCAM SA3, Photron USA, Inc.) at 1,000 frames per second and 512×256 pixels resolution. Among the three subjects, one is a snorer and the other two are not. The usage of *in vivo* images has been approved by the institutional review board at California Baptist University. Fig. 1c shows the uvula position at eight instants in one flapping period of a non-snorer, who is supposed to have a normal sized uvula (Hamans et al., 2000). Due to technical limitations, only the front view of the uvula motion can be captured using an externally positioned camera. However, the trajectory of the uvula tip still clearly exhibits a sinusoidal waveform. Differences were also noted in the amplitude of tip excursion (E), which can be similar to the midpoint amplitude (heaving mode), or much larger (pitching mode). Based on the slow-motion analysis results, a virtual skeleton bound with the uvula model was introduced to reconstruct the uvula kinematics in Autodesk® Maya® (Autodesk Inc.) (Fig. 1d). Two ball joints were used to control the motions of the uvula at its root and midpoint, respectively. Same technique has been successfully applied to the kinematics reconstructions of birds (Wang et al., 2019) and fish (Liu et al., 2017). In this study, two uvula flapping modes were reconstructed, including the heaving mode and the pitching mode, as shown in Fig. 1f *vs.* g. The rotation angles of the root (θ_R) and middle (θ_M) joints for the heaving and the pitching mode were prescribed in Eqs. (1)&(2), respectively.

$$\theta_R = \Phi_H \sin(2\pi t/T), \theta_M = \Psi_H \sin(2\pi t/T + \pi); \Phi_H = \Psi_H = 20^\circ. \quad (1)$$

$$\theta_R = \Phi_P \sin(2\pi t/T), \theta_M = \Psi_P \sin(2\pi t/T); \Phi_P = \Psi_P = 15^\circ. \quad (2)$$

where Φ and Ψ are the angle amplitudes of the root and the middle joints, respectively. The 15° Φ_P and Ψ_P for pitching mode were measured based on the dynamic MRI data shown in Fig. 1b. The 20° Φ_H and Ψ_H for heaving mode were chosen so that the heaving uvula's centroid of volume matches with that of the pitching mode at maximum flapping amplitude, and a fair comparison between the two modes can be made. The phase lag π in Eq. (1) was added so that the root joint and middle joint were out of phase and the heaving mode of uvula flapping was created.

To investigate the effects of pharynx width on the aerodynamics in OSA, the pharynx was constricted to simulate a narrowed airway. Fig. 1e&f show the comparison of the airway morphologies between the normal and the constricted pharynx. The ratios of the cross-sectional area (A_P) and the pharynx width (W) between the normal and the constricted pharynx were 3.5 and 2.4, respectively. Pressure probes were distributed at three points of interest in the airway to monitor the pressure change in the airflow (Fig. 1e–h).

To study the uvular frequency effects, three flapping frequencies of the uvula (50, 100, 200 Hz) were tested in comparison to a stationary model. The base flapping frequency followed the experimental study (Miyazaki et al., 1998) to be 100 Hz. The peak inhalation flow rate was assumed to be 20 L/min, which is close to the peak inspiratory flow rate range of 22.2–24.0 L/min of seven habitual snorers during sleeping reported by (Clark et al., 1998). To simulate the concurrent oronasal breathing during sleep, 80% of the air enters through the nose while 20% through the mouth.

Table 1 summarizes the changes in the key parameters involved in this study and their ranges. The Reynold number ranged from 997 to 1188.

2.2. Numerical methods

The governing equations solved in this work are the incompressible Naiver-Stokes equations, written as:

$$\frac{\partial u_i}{\partial x_i} = 0; \quad \frac{\partial u_i}{\partial t} + \frac{\partial u_i u_j}{\partial x_j} = -\frac{\partial p}{\partial x_i} + \frac{1}{Re}\frac{\partial^2 u_i}{\partial x_i \partial x_j} \quad (3)$$

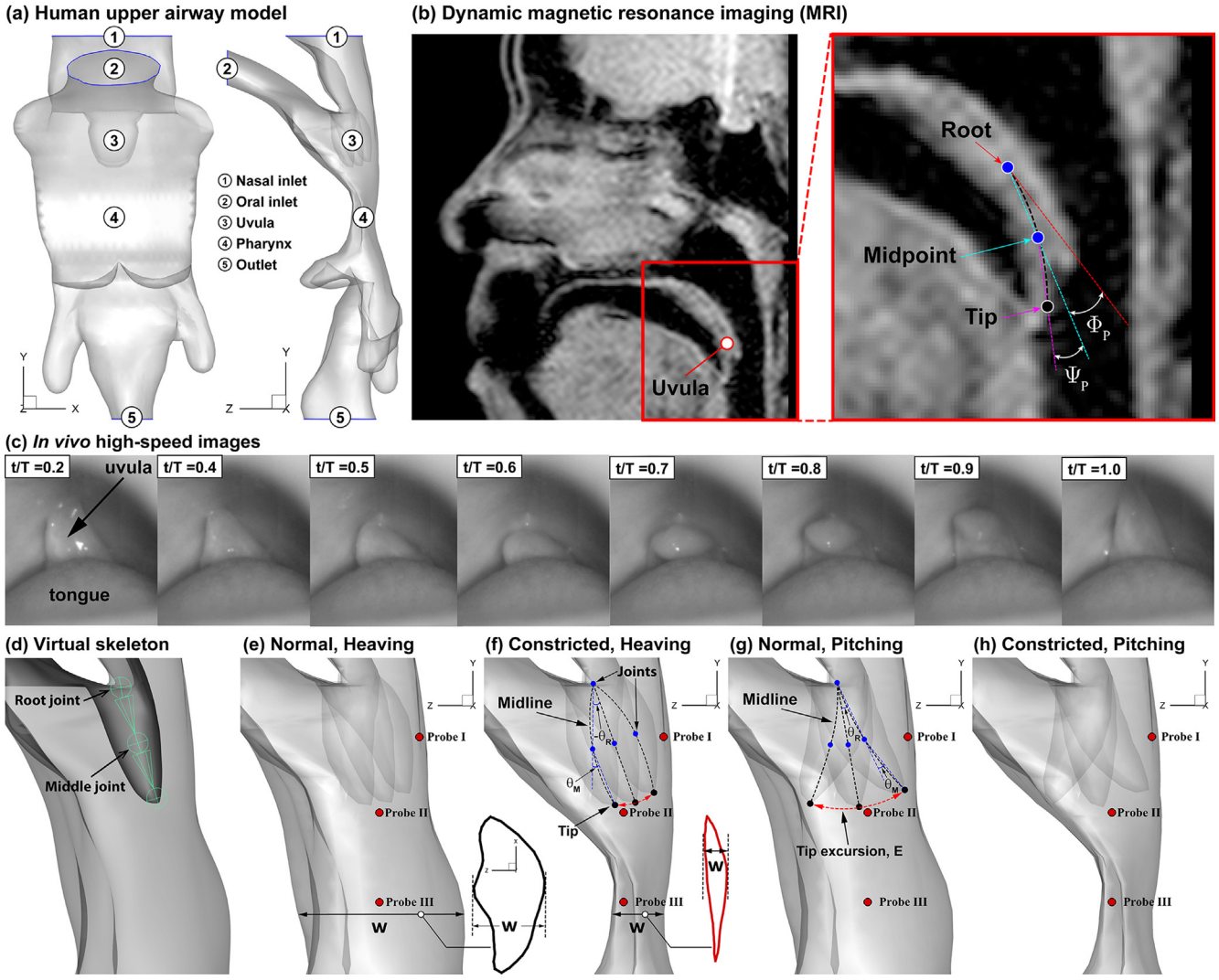

Fig. 1. (a) Detailed views of the computational model. The model includes two air inlets (nasal and oral) and one outlet. In the side view (right), uvula positions at three time-instants are shown. (b) Dynamic magnetic resonance imaging (MRI) data with measurements of uvula angles Φ_P and Ψ_P at root and midpoint, respectively, on mid-sagittal plane at maximum uvula flapping amplitude. The black-dashed line denotes uvula midline. (c) High-speed camera images of uvula kinematics in one flapping cycle. (d) virtual skeletons adopted for uvula kinematics reconstruction. The virtual skeleton was smoothly bound with the uvula mode. Two ball joints, including the root joints and the middle joints are connected by virtual bones. (e–h) Comparison of airway width between the original pharynx (e) and the constricted pharynx (f), and the comparison of uvula kinematics between the heaving mode (f) and the pitching mode (g). The midline and the tip of the uvula are denoted with black dashed line and black dot, respectively. The blue dots denote the locations of the joints. θ_R and θ_M are the rotation angles of the root and middle joints, respectively. E denotes the peak-to-peak tip excursion of the uvula. The black and red outlines show the shapes of the cross-sections of the normal and the constricted pharynx. W denotes the pharynx width. The three pressure probes are marked as red dots with a black outline. (For interpretation of the references to colour in this figure legend, the reader is referred to the web version of this article.)

Table 1
Key parameters involved in this study and their ranges.

Morphology	Flapping mode	f(Hz)
Normal pharynx (W = 0.20L), Constricted pharynx (W = 0.08L)	Heaving mode (E = 0.08L), Pitching mode (E = 0.15L)	0(stationary), 50, 100, 200

where u_i are the velocity components and p is the pressure. For solving airflows in human airway, an in-house immersed-boundary-method (IBM) based direct-numerical-simulation (DNS) solver (Mittal et al., 2008) was employed, which has been successfully applied to biological flapping propulsions including insects (Bode-Oke et al., 2018), birds (Wang et al., 2019), and fish (Liu et al., 2017). Recently, it has been validated against various CFD solvers, including laminar model, RANS, and LES, in simulating human nasal airflow (Li et al., 2017).

The computational domain (Fig. 2a) had the size of $0.6L \times 1.0L \times 0.4L$ with a grid size of 5.3 million ($161 \times 257 \times 129$). The inner airway surface was represented by an unstructured mesh with triangular elements, on which the boundary conditions were imposed using the multi-dimensional ghost-cell method (Dong et al., 2006). Two velocity inlets (nasal and oral) and one pressure outlet (trachea) were applied. Zero-gradient boundary condition was applied to the outlet to allow the convection of the vortices without significant reflection. The primitive variables u_i and p were discretized on the Cartesian grids using a second-order center-difference scheme in space. A second-order accurate fractional-step time-marching scheme was employed.

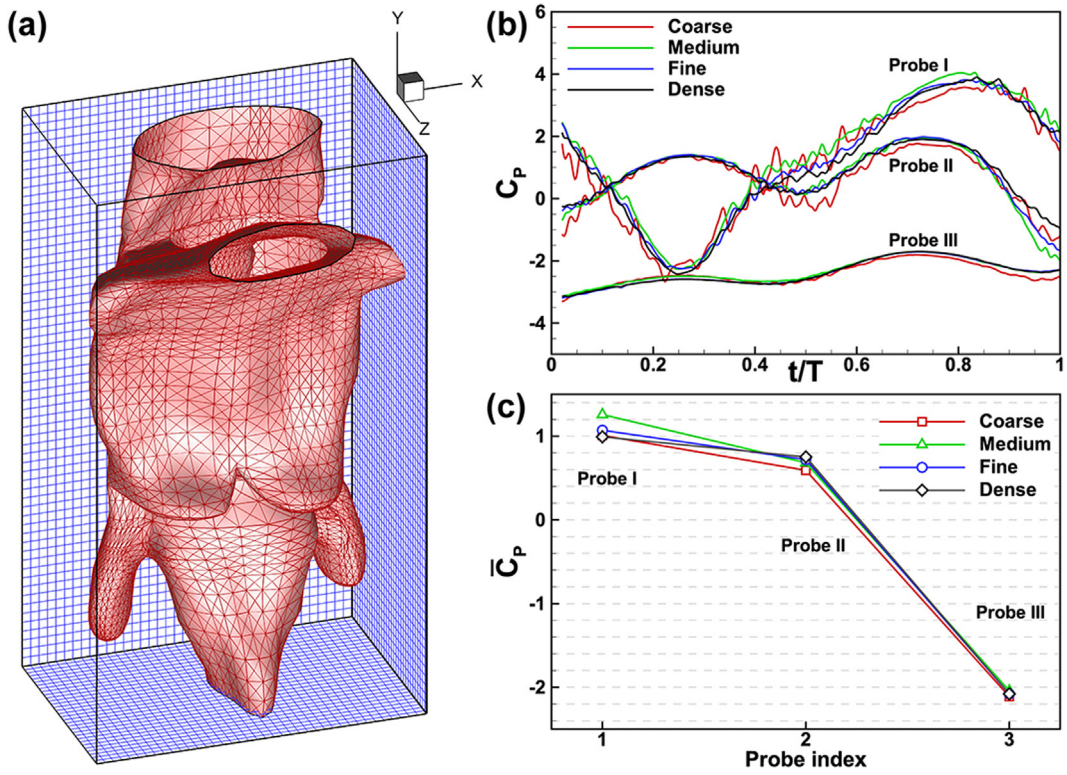

Fig. 2. (a) Typical triangular mesh (in red) and computational grid (in blue) employed in the current simulations for the airway-uvula system model. (b&c) Grids independent study of the instantaneous (b) and cycle-averaged (c) pressure coefficient, respectively, at three probes. The minimum grid spacings of the coarse, medium, fine, and dense meshes are 0.0059L, 0.0039L, 0.0029L, and 0.0023L, respectively. (For interpretation of the references to colour in this figure legend, the reader is referred to the web version of this article.)

2.3. Wavelet transform and variance analysis

Continuous wavelet transform (CWT) analysis was performed to decompose the time history of pressure signal at the three probes. Details on the methodology of CWT used in this paper and the reason for using CWT analysis can be found in Appendix A.

3. Results

The simulation results, including the probe pressure, vortex structures, and surface pressure/forces are presented and compared across the simulations. The 3-D vortex structures are visualized using isosurfaces defined by Q-criterion (Hunt et al., 1988), with $Q = \frac{1}{2}\left[|\Omega|^2 - |\Lambda|^2\right] > 0$. Here $\Lambda = \frac{1}{2}[\Delta \boldsymbol{u} + (\Delta \boldsymbol{u})^{\mathrm{T}}]$ and $\Omega = \frac{1}{2}[\Delta \boldsymbol{u} - (\Delta \boldsymbol{u})^{\mathrm{T}}]$ are the shear strain rate and vorticity tensors, respectively. The instantaneous pressure coefficients C_P at probes and the nondimensional force F_Z on the pharyngeal wall were calculated as,

$$C_P = \frac{p}{\frac{1}{2}\rho U_{out}^2}, F_Z = \frac{F_p}{\frac{1}{2}\rho U_{out}^2 L^2} \tag{4}$$

where p is the gauge pressure, U_{out} is the mean outlet flow velocity, and F_p is the z-component of the pharyngeal wall force caused by pressure. L is the height of the pharynx part of the human airway model used in the present study, and $L = 92$ mm.

Convergence studies have been conducted to prove the present results are independent of computational grids. Four sets of grids, including the coarse (0.8 million), medium (2.8 million), fine (5.3 million), and dense (9.0 million) grids, were employed. Fig. 2b&c shows both the instantaneous (C_P) and cycle-averaged ($\bar{C}_P$) pressure coefficients converged as the grids number increased at all three probes. The differences between the fine and the dense meshes were minimal (less than 3% in $\bar{C}_P$ at probe II). The present simulations all adopted the fine grid, which has 22 grid points across the smallest cross-section of the narrowed pharynx model.

3.1. Effect of pharynx width

Fig. 3 compares the instantaneous vortex structures (Q-criterion, Q = 80) in the pharyngolaryngeal airways between the normal and the constricted pharynx at four time-instants with a heaving uvula. Large amount of vortices induced by the flapping motions of the uvula were observed in both models. The vortices decayed quickly as they were transported downstream in the normal pharynx. By contrast, in the constricted pharynx, they were amplified by the narrow duct and continued to grow after exiting the narrowing, causing more intensified vortices in the pharyngolaryngeal region.

Fig. 4 compares the energy contents (wavelet variance) between the normal and the constricted pharynx in terms of different frequencies at three probes. For all probes, pressure oscillations over the scale of 50–400 Hz accounted for most of the variability in the time series. Comparing normal and constricted, however, more differences in energy intensity were found when the probe was located more downstream, indicating the constriction significantly changed the aerodynamic pressure behaviors downstream the uvula. The variance at the 2nd-harmonic, relative to the fundamental frequency, also increased from probe I to III, indicating pressure fluctuations more dominated by the flapping motions of the uvula in the downstream.

The above results were also verified by breaking the probe signals into frequency-specific time series components (shown in the

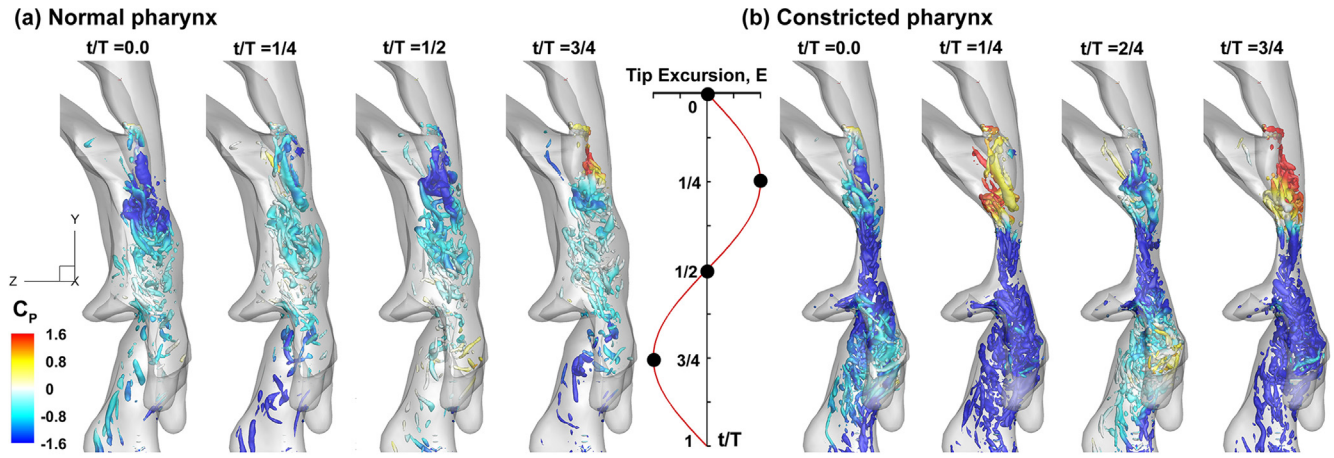

Fig. 3. Comparison of airway vortex structures at four time-instants (t/T = 0, 0.25, 0.5, and 0.75) between the normal (a) and the constricted pharynx (b) from side views. Three-dimensional wake topologies are visualized using the Q-criterion (Q = 80). The isosurfaces are flooded by C_P.

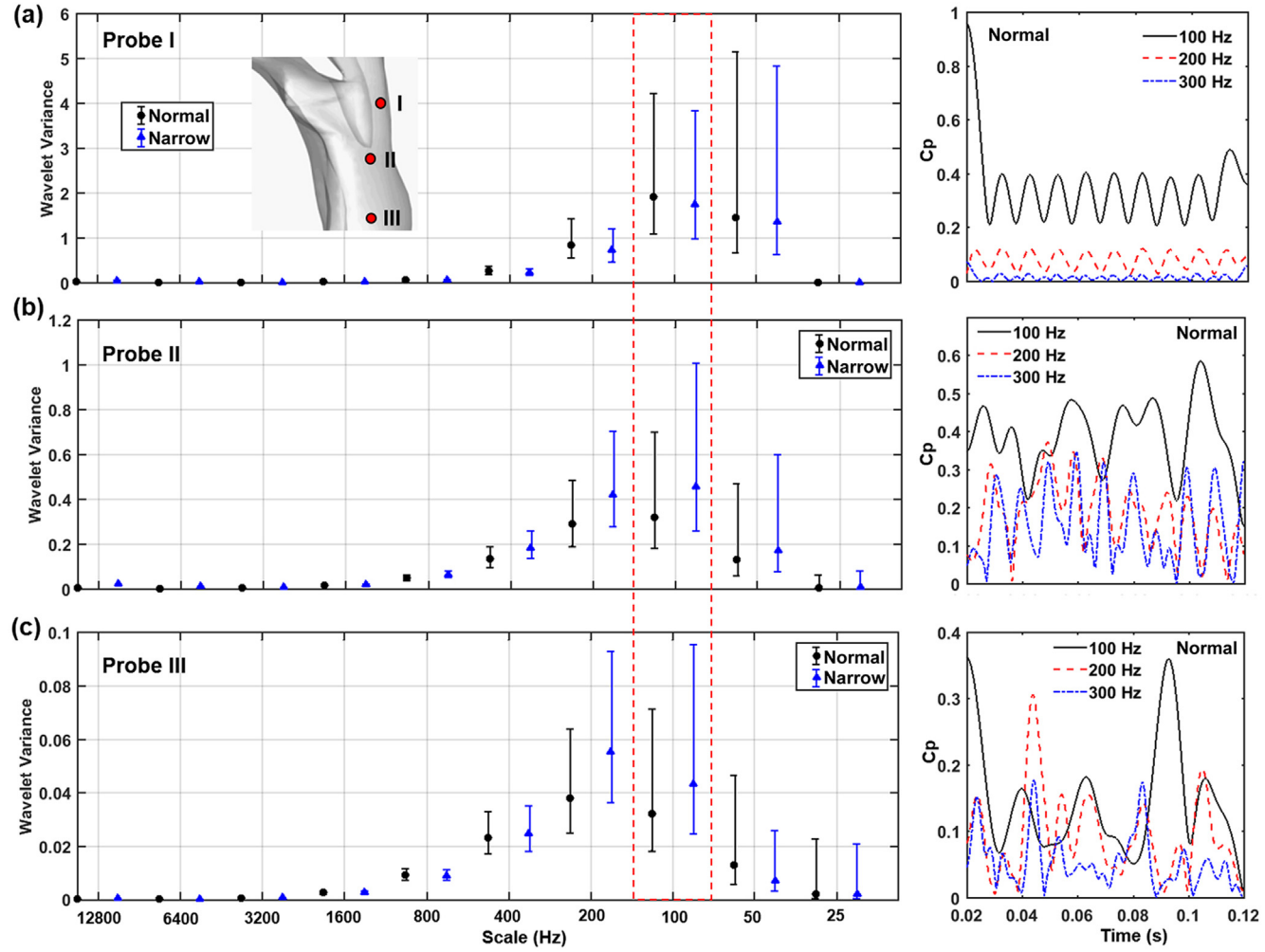

Fig. 4. Comparison of energy spectrum between models with the normal and the constricted pharynx at three locations: (a) probe I, (b) probe II, and (c) probe III. The left panels show the wavelet variance at different frequency scales; the right panels show the frequency-specific components of the probe pressure time series of the normal pharynx at three frequencies (100 Hz, 200 Hz, and 300 Hz).

right panels of Fig. 4). From probe I to III, the sinusoidal waveforms became more irregular and the signal intensity at higher frequencies (200&300 Hz) increased, mainly because of the interplay between the vortex shed from the uvula and the turbulent shear layers from the airway walls, observed in Fig. 3.

3.2. Effect of uvula flapping mode

Fig. 5a compares the streamwise velocity at the midsagittal plane of the airway between the heaving and the pitching uvula at their leftmost positions. A strong reverse jet formed to the left

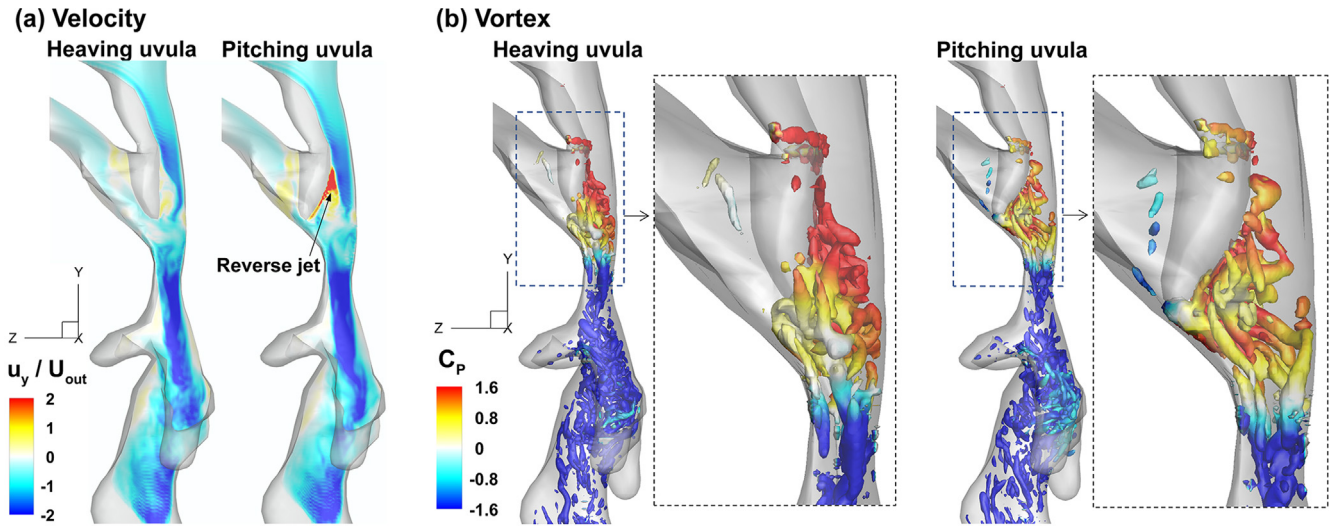

Fig. 5. Comparison of the velocity field and vortex structures between the heaving and the pitching uvula when the uvula was at the leftmost position: (a) instantaneous velocity at the middle plane of the airway and (b) instantaneous coherent structures and zoom-in views around the uvula. The velocity is scaled by the mean velocity at the outlet. The vortex was colored by the pressure coefficient C_P. (For interpretation of the references to colour in this figure legend, the reader is referred to the web version of this article.)

of the pitching uvula due to the adverse pressure gradient caused by flow separation. In contrast, no obvious reverse jet was found in the heaving uvula.

Fig. 5b demonstrates that different vortex patterns were captured by the IBM-based DNS simulations between different uvula flapping mode. Due to complex anatomical details such as airway constriction and hanging/protruding/dynamic structures, different flow phenomena coexisted. For example, wall shear flow, vortex shedding, flow separation/reattachment, and their dynamic interplay. Vortex shedding from the back of the uvula appeared to be more dominating than other mechanisms. These coherent structures were subsequently transported to the pharynx and larynx, leading to various levels of flow instability and turbulence.

The cycle-averaged pressure coefficients ($\bar{C}_P$) at probes II&III were 0.61 and −1.75 for the heaving uvula and 0.57 and −1.84 for the pitching uvula, respectively, showing small differences in $\bar{C}_P$ downstream the uvula caused by two uvula flapping modes.

3.3. Effect of uvula flapping frequency

The dynamic MRI and high-speed image (Fig. 1b&c) showed the significant flapping motion of uvula, which will inevitably cause unsteady effects to the airflow. However, few literatures has included a dynamic uvula in upper airway simulations. In this section, the aerodynamics of a fixed uvula is studied and compared with flapping uvulas at various flapping frequencies, so that the aerodynamic impact of a flapping uvula can be examined. The uvular frequency effects on airflows and pressure fluctuations in the pharyngolaryngeal airway are shown in Fig. 6. Similarities, as well as large discrepancies, were noted in the x-vorticity fields among different uvula flapping frequencies (Fig. 6a–d). For all frequencies, the constricted pharynx caused the flow shear layers that detached from the airway wall (black arrows in Fig. 6a) to interact with vortices shed from the uvula. The shear layers were stable when the uvula was stationary (Fig. 6a). They became unstable and oscillatory as the frequency increased and eventually broke into even finer vortices (red ellipse in Fig. 6c). Earlier breakups were noted at 200 Hz than 100 Hz, indicating a more unstable flow at higher frequencies.

Even more significant differences due to frequency effects were detected in the vicinity of the uvula (blue rectangles in Fig. 6a&d). With increasing flapping frequency, the vorticity field in this region progressively increased in complexity, and the vortex sizes became finer. Fig. 6d reveals a multi-layer vorticity field formed to the left of the uvula: the first layer (1, blue) resulted from the vacuum at the back of the flapping uvula, the second layer (2, red) was the remnant of the shear layer from the left wall of the uvula, while the third layer (3, blue) resulted from the shear layer separated from the front wall of the uvula, which curved up due to the fast, right-flapping motion of the uvular tip. A similar pattern was also found at 50 and 100 Hz, but at much-reduced intensities (Fig. 6b&c).

Fig. 6e compares C_P between various flapping frequencies (0, 50, 100, and 200 Hz) at probes I&II, respectively. The pressure was relatively steady at all probes when the uvula was stationary. The fluctuations intensified continuously as the uvula flapping frequency increased from 0 to 200 Hz, regardless of the probes' location.

The pressure signals at probe II was further analyzed using FFT and CWT for 50, 100, and 200 Hz (Fig. 7). All three FFT spectrums exhibited peaks at the fundamental frequency and its harmonics (2nd to 4th), which together dominated the signal energy. However, nonlinear responses of the flow to the external forcing (here uvula oscillation) were found in terms of the energy distribution *vs.* frequency (Fig. 7a). The amplitude ratio between the 2nd-harmonic and the base frequency increased from 0.26 to around 1.0 as the flapping frequency increased from 50 to 200 Hz. Note, the absolute amplitudes at 200 Hz were more than twice those at 50 and 100 Hz.

Fig. 7b shows the scalograms at the three frequencies after CWT analysis of the pressure probe signals. In this way, temporal variations of the energy spectrum can be clearly viewed. All scalograms exhibited a clear periodicity when $f/F_0 > 8$, with a frequency that was twice of the forcing frequency, as evidenced by the dashed rectangle (Fig. 7b). Moreover, high energy was only found at the fundamental frequency ($f/F_0 = 1$) for the 50 Hz case, while it was found at $f/F_0 = 1$–2 for 100 Hz, and at $f/F_0 = 1$–4 for 200 Hz, which corroborated the FFT results in Fig. 7a.

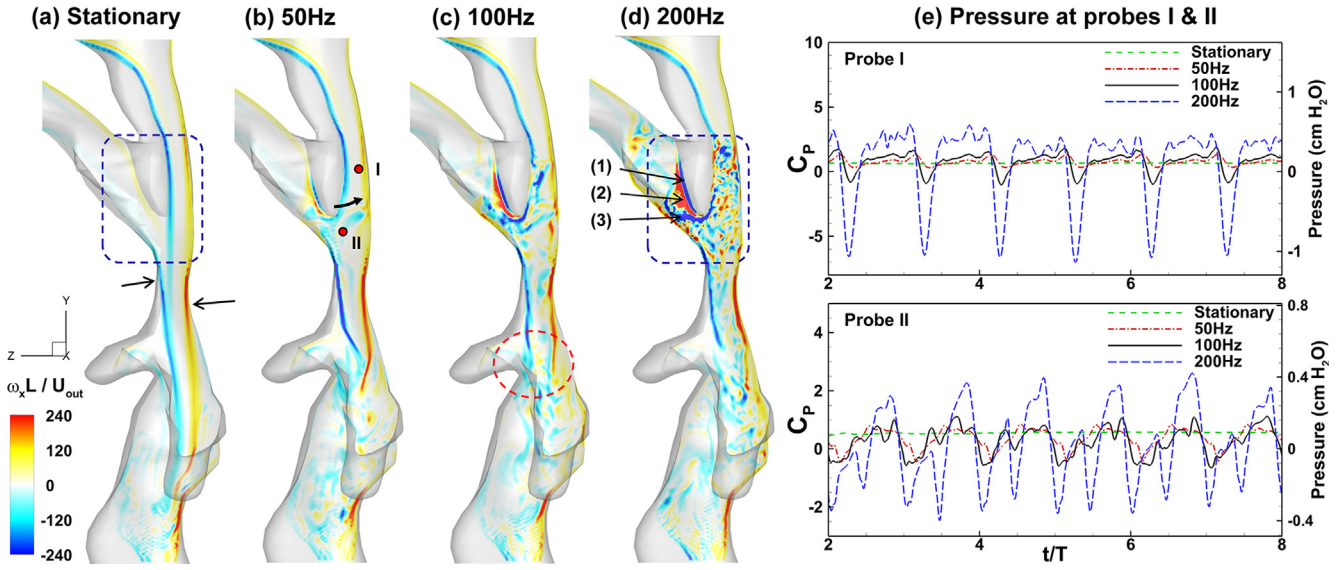

Fig. 6. Comparison of x-vorticity on slice-cuts at the median plane of the constricted pharynx model with the pitching uvula under different uvula flapping frequencies: (a) 0 Hz (stationary), (b) 50 Hz, (c) 100 Hz, and (d) 200 Hz. Comparison of pressure at probes I and II among different uvula flapping frequencies is shown in (e).

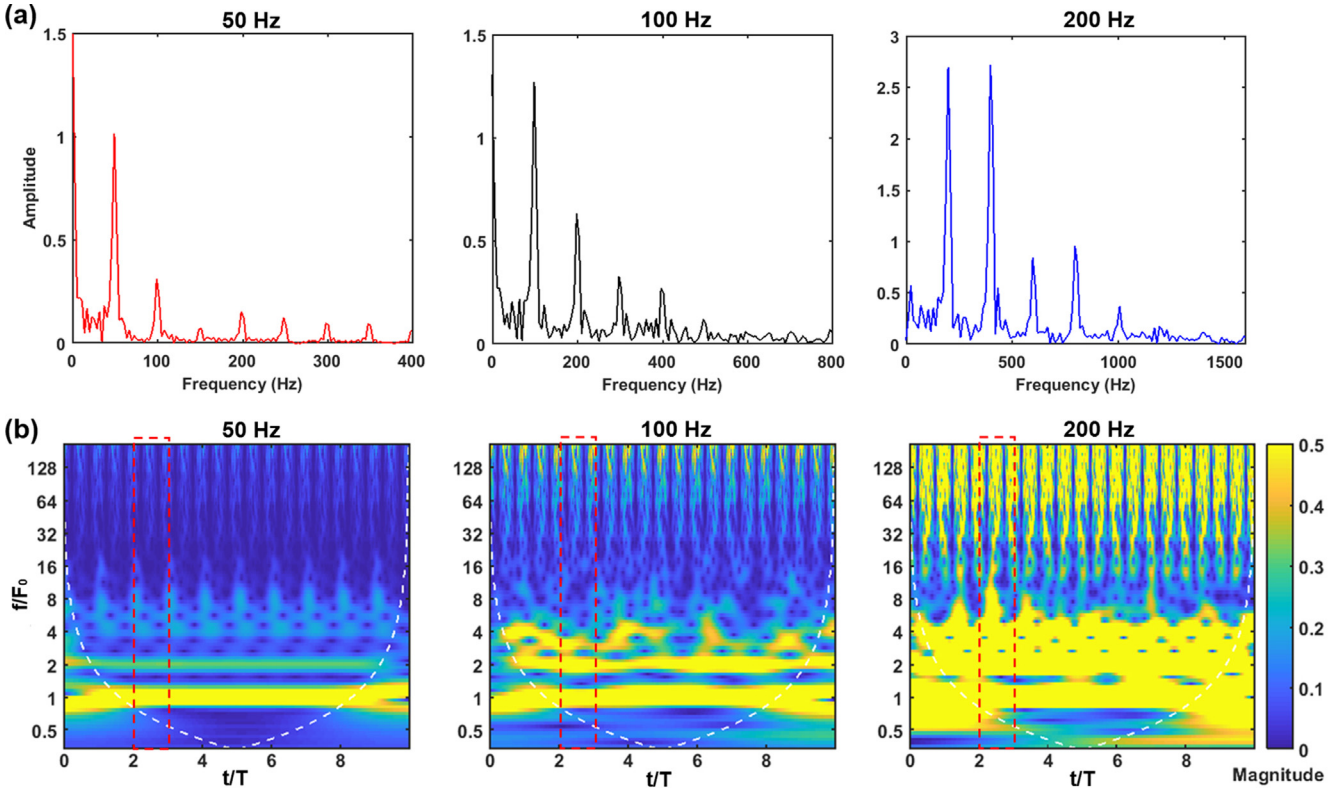

Fig. 7. Pressure signal analysis at Probe II in the constricted model with the pitching uvula under different uvula flapping frequencies: (a) fast Fourier transformation (FFT) and (b) scalogram based on continuous wavelet transformation (CWT).

3.4. Pharyngeal wall collapsibility

Fig. 8 compares the C_P distribution on the pharyngeal back walls between the normal and the constricted pharynx at four time-instants. Significant pressure difference at corresponding regions were found. As expected, the upper wall (red box) in constricted pharynx had higher pressure than in the normal one, while the lower part (blue box) had lower pressure, being consistent with probe pressure results in the previous study (Wang et al., 2018). The upper wall had the lowest pressure at t/T = 0.25 when the uvula was rightmost (closest to the back wall) and the highest pressure at t/T = 0.75 when leftmost, showing the direct influence of uvula motions on the wall pressure distribution.

The region of interest (RoI) (Fig. 9a) had a height of 1.4 cm covering the most collapsible region of the pharynx. Consistently negative pressures were observed in the RoI of the constricted passage

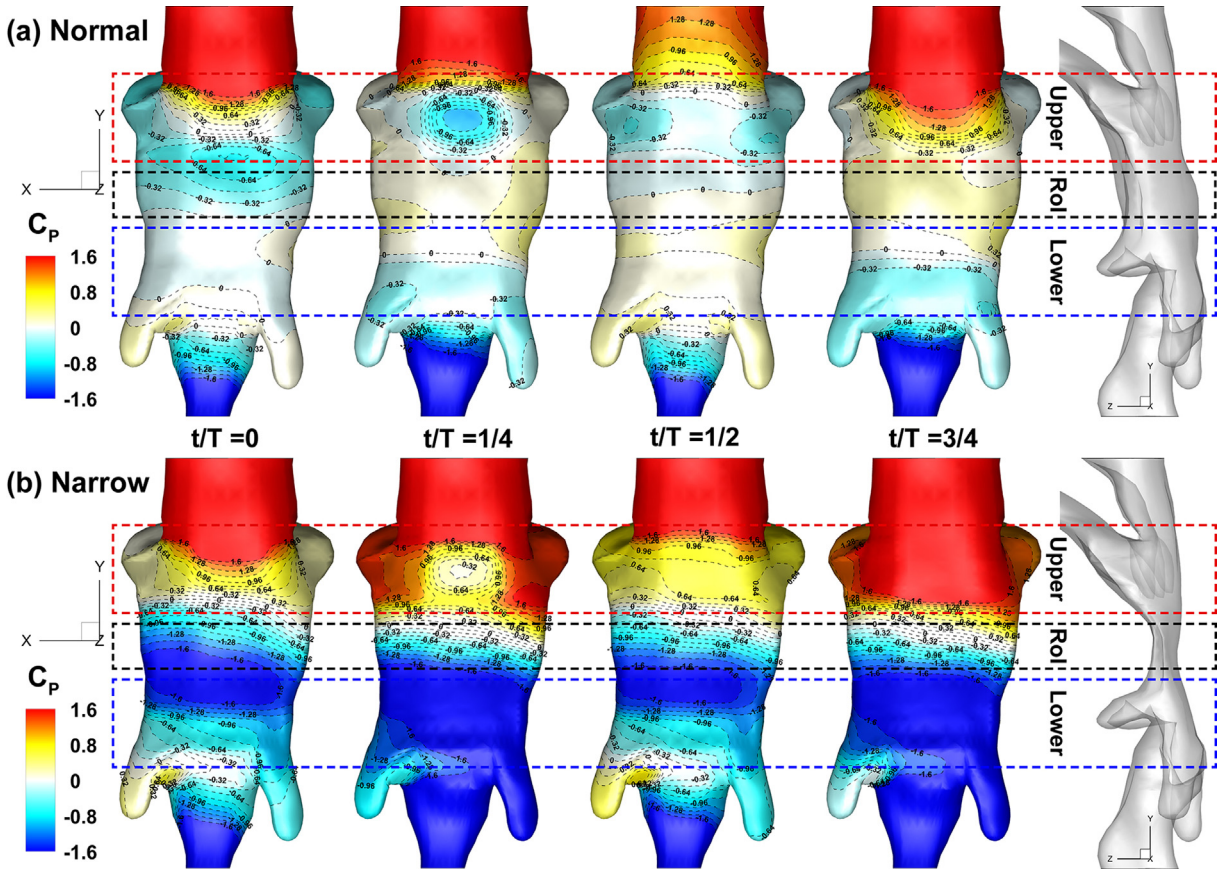

Fig. 8. Comparison of the pharyngeal wall pressure distribution between the normal (a) and the constricted pharynx (b) at four time-instants (t/T = 0, 0.25, 0.5, and 0.75). The dashed boxes in red and blue denote the upper and lower part of the pharynx, respectively. The dashed box in black represents the region of interest (RoI) corresponding to the narrowest part of the constricted pharynx. (For interpretation of the references to colour in this figure legend, the reader is referred to the web version of this article.)

(Fig. 8b). As a result, a normal force pointing toward the airway lumen was predicted on both the front and back pharyngeal walls (Fig. 9b), promoting collapse of the pharynx. The collapse would further narrow the air passage, leading to higher collapsibility and eventually complete airway closure (OSA). In contrast, the force of the normal airway passages varied along zero and alternated directions on both the front and back walls (Fig. 9b), lending a possibility of wall vibrations for over-compliant walls. Fig. 9e shows the mean values and standard deviations of the force histories in Fig. 9b. Besides the dramatic change in the mean wall forces between the normal and the constricted pharynx, the standard deviations of the forces also increased, indicating greater force fluctuations due to the constriction. The time-averaged pressure at Probe III in the RoI is around $-2.4\ cmH_2O$ which corresponds to an electromyographic (EMG) activation threshold level of 4% in OSA patients and a 1.3 mm soft palate displacement modeled by (Liu et al., 2019), indicating an early stage of airway collapse.

Similar mean forces were found in the RoI between the heaving and the pitching uvula (Fig. 9c), showing insensitivity of the mean wall forces to the uvula flapping mode. However, the standard deviations of the heaving uvula were larger than the pitching one (Fig. 9f), showing more force fluctuations, reaffirming the finding from probe pressures in the previous study (Wang et al., 2018).

The flapping frequency of uvula has significant impacts on the wall force exerted on RoI. The forces were nearly constant on both the front and back walls when the uvula was stationary (Fig. 9d). As the flapping frequency increased, both the mean values and the standard deviations of the wall forces increased monotonically (Fig. 9g). The force oscillations increased dramatically from 100 Hz to 200 Hz (Fig. 9d), resulting in a 262% and a 265% standard deviation increase in the front and back walls of RoI, respectively (Fig. 9g). The results suggest that the flapping frequency of the uvula was a dominant factor in determining the fluctuations of the forces on the pharyngeal wall.

4. Discussion

The present study has demonstrated significant effects of uvula kinematics on airflows, pressure fluctuations, and pharyngeal wall forces during snoring/OSA, which has not been reported before. The uses of high-speed photography, anatomically accurate model, and high-fidelity DNS flow solver has greatly promoted the credibility of this work.

Results of this study would help better understand the pathology of snoring/OSA from an aerodynamic perspective. The current results indicate that there might exist a threshold of the airway constriction, wider than which only wall vibrations are possible (snoring) while narrower than which a cascade of wall collapse would happen, leading to OSA (Fig. 9). Many factors can affect this airway passage threshold, such as the vibration frequency of the uvula, the respiration flow rate, and the compliance of the pharynx wall. Alternatively, guidance can be learned to intervene symptoms of snoring/OSA. For OSA, if the airway opening can be sustained above the threshold level, then the initiation of airway collapse can be avoided. One example is the CPAP (continuous positive airway pressure) machine for OSA patients that uses positive pressures to keep the airway open (Stuck et al., 2012). For snoring,

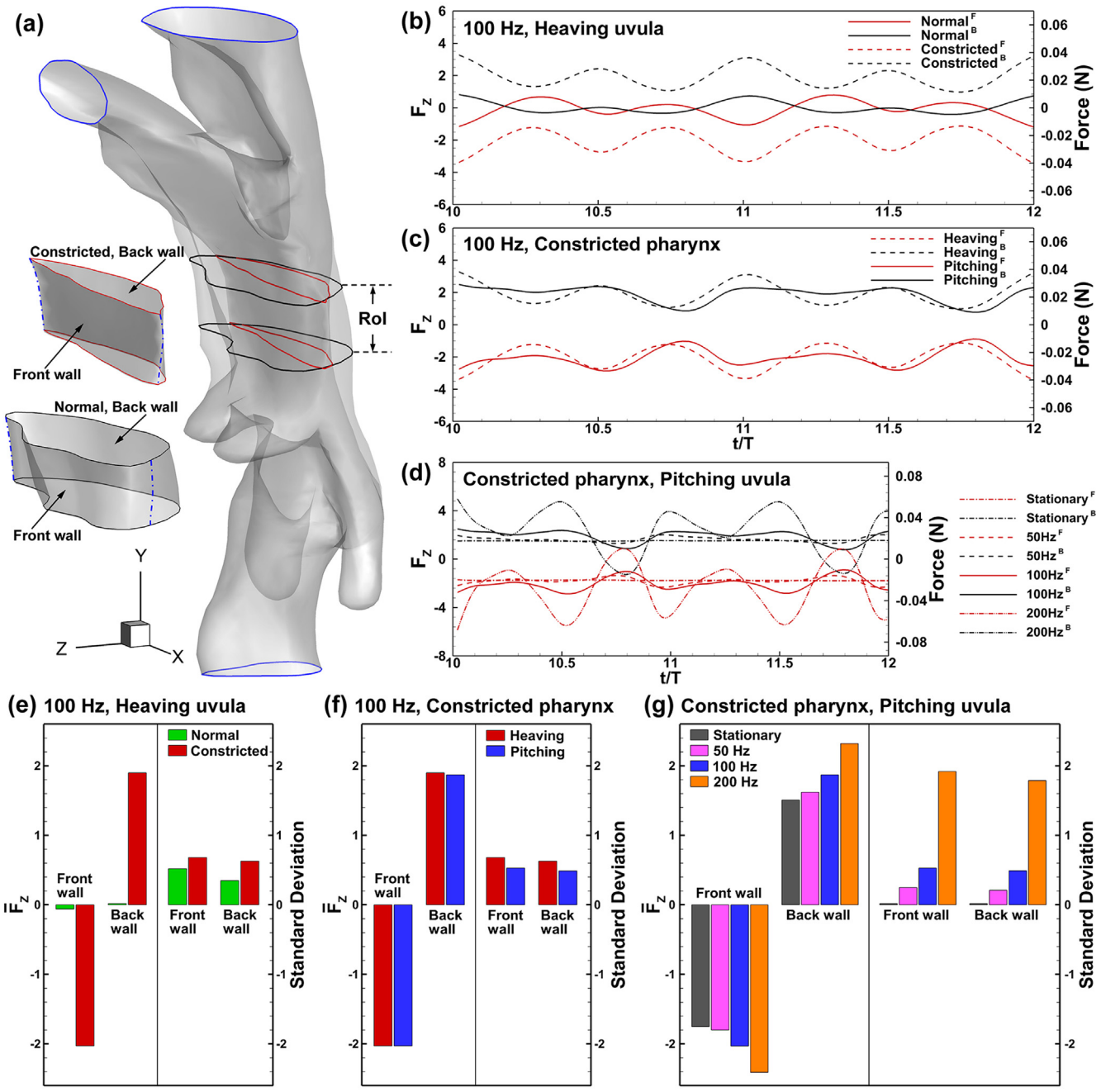

Fig. 9. Forces on the pharyngeal front and back walls caused by pressure: (a) Region of interest (RoI) in the normal and the constricted pharynx, respectively. (b–d) Comparison of pharyngeal wall force between the normal and the constricted pharynx (b), between the heaving and the pitching uvula (c), and between various uvula flapping frequencies (Stationary, 50 Hz, 100 Hz, and 200 Hz) of the constricted pharynx with pitching uvula (d). In (a) each RoI contains a front wall and back wall separated by blue dash-dot lines. In (b–d), red lines denote forces exerted on the front wall and black lines on the back wall. (e–g) Mean values and standard deviations of the corresponding wall force time histories in (b–d). (For interpretation of the references to colour in this figure legend, the reader is referred to the web version of this article.)

since the flapping frequency of the uvula is determined by its natural (resonance) frequencies, as shown in the FSI study (Pirnar et al., 2015), somnoplasty procedures such as fiber implants, fat injection, and section/removal of the uvula (Madani, 1999; Srinivasan et al., 2008) can be used to alter the natural frequency and eventually to prevent or reduce uvula vibrations (Cartwright et al., 2000; Javaheri and Wexler, 2005).

Limitations of this study include the assumptions of rigid airway walls and the idealized and prescribed kinematics of the uvula. More detailed discussion on the limitations is in Appendix B.

5. Conclusion

In this study, a physiologically based upper airway model with varying uvular kinematics was developed. Direct numerical simulations of flow dynamics inside the airway were conducted using an immersed boundary method. It was observed that both vortex development and aerodynamic pressure were highly sensitive to the level of airway constriction, while were insensitive to the uvula flapping mode if the flapping frequency were identical. A partially constricted pharynx was prone to cause further collapse of a

flexible airway. Pressure oscillations were in phase with the uvular base oscillations, and also exhibit oscillation features at higher orders of harmonics. Moreover, the frequency of uvular oscillation was found to be a dominant factor in determining the amplitudes of airway pressure fluctuations and pharyngeal wall force oscillations.

Declaration of Competing Interest

To the best of our knowledge, no conflicts of interest exist for any of the authors.

Acknowledgments

This study was funded by NSF, USA grant CBET-1605232 and NSF grant CBET-1605434. Mohamed Talaat is gratefully acknowledged for reviewing the manuscript.

Appendix A

Wavelet transform and variance analysis

Wavelet transform can decompose a time series pressure signal into different scales to detect relationships not obvious in the original data. It uses a family of wavelets by translating and dilating a mother wavelet, expressed as:

$$wt(a,b) = \frac{1}{\sqrt{a}} \int_{-\infty}^{\infty} f(t)\psi\left(\frac{t-b}{a}\right)dt, a > 0 \quad \text{(A.1)}$$

where $\psi(t)$ is the mother wavelet (analysis window), $f(t)$ is the temporal variation of the signal, a is the variable that controls the expansion or compression the mother wavelet, and b is a time lag. Local irregularities can be extracted by varying the two variables a and b (Grossmann and Morlet, 1984). In this study, continuous wavelet transform (CWT) was performed to identify the time–frequency spectrum (scalogram) and signal variance. The Haar wavelet was selected as the mother wavelet for both analyses (Grossmann and Morlet, 1984).

The reason for using CWT analysis is because the airway pressure behaves differently in terms of magnitude and frequency at varying flapping frequencies of the uvula. The highest energy component of airway pressure, which is most responsible for the airway collapse, does not always occur at the uvula flapping frequency, but may occur at its second or third harmonics. Wavelet analysis provides this information by breaking the pressure into energy components at different frequencies (i.e., energy spectrum) and helps to identify both the amplitudes and frequencies of the high-energy components. Moreover, insights into the nonlinear interaction between the uvula and airflow can be gained through examining the energy spectrum and its temporal variation.

Appendix B

Limitations of this study include the assumptions of rigid airway walls and the idealized and prescribed kinematics of the uvula. However, this study aimed to quantitatively evaluate the impacts of uvula oscillations and airway constriction on pharyngeal wall collapsibility, not the snoring process. Using the rigid wall assumption will not fundamentally change the force behavior on the pharyngeal wall due to uvula oscillations. In addition, using these assumptions significantly reduced computational demands. Future investigations on sleep apnea using two-way fluid–structure interactions are needed to gain deeper insights into the mechanisms of snoring and sleep apnea so that the coupling between aerodynamic force and structural dynamics can be fully solved. It is noted that DNS simulations of respiratory aerodynamics with dynamic structures are still numerically complicated and computationally expensive. With a computational mesh of 5.3 million and a time step size of 2.0e-5 s, one simulation with 0.12 s (12 cycles) took approximately 189 h (8 days) in an Intel® Xeon® E5-2609 v2 workstation.

References

Arens, R., McDonough, J.M., Corbin, A.M., Rubin, N.K., Carroll, M.E., Pack, A.I., Liu, J., Udupa, J.K., 2003. Upper airway size analysis by magnetic resonance imaging of children with obstructive sleep apnea syndrome. Am. J. Respir. Crit. Care Med. 167, 65–70.

Ayappa, I., Rapoport, D.M., 2003. The upper airway in sleep: physiology of the pharynx. Sleep Med. Rev. 7, 9–33.

Bode-Oke, A.T., Zeyghami, S., Dong, H., 2018. Flying in reverse: kinematics and aerodynamics of a dragonfly in backward free flight. J. Royal. Soc. Interf. 15, 20180102.

Cartwright, R., Venkatesan, T.K., Caldarelli, D., Diaz, F., 2000. Treatments for snoring: a comparison of somnoplasty and an oral appliance. Laryngoscope 110, 1680–1683.

Clark, S.A., Wilson, C.R., Satoh, M., Pegelow, D., Dempsey, J.A., 1998. Assessment of inspiratory flow limitation invasively and noninvasively during sleep. Am. J. Respir. Crit. Care Med. 158, 713–722.

Dong, H., Mittal, R., Najjar, F., 2006. Wake topology and hydrodynamic performance of low-aspect-ratio flapping foils. J. Fluid Mech. 566, 309–343.

Fajdiga, I., 2005. Snoring Imaging: could bernoulli explain it all? Chest 128, 896–901.

Grossmann, A., Morlet, J., 1984. Decomposition of hardy functions into square integrable wavelets of constant shape. SIAM J. Math. Anal. 15, 723–736.

Hamans, E.P.P.M., Van Marck, E.A., De Backer, W.A., Creten, W., Van de Heyning, P. H., 2000. Morphometric analysis of the uvula in patients with sleep-related breathing disorders. Eur. Arch. Otorhinolaryngol. 257, 232–236.

Henrik Strand Moxness, M., Wülker, F., Helge Skallerud, B., Nordgård, S., 2018. Simulation of the upper airways in patients with obstructive sleep apnea and nasal obstruction: a novel finite element method. Laryngoscope Investigat. Otolaryngol. 3, 82–93.

Huang, R., Li, X., Rong, Q., 2013. Control mechanism for the upper airway collapse in patients with obstructive sleep apnea syndrome: a finite element study. Sci. China Life Sci. 56, 366–372.

Huang, Y., Malhotra, A., White, D.P., 2005. Computational simulation of human upper airway collapse using a pressure-/state-dependent model of genioglossal muscle contraction under laminar flow conditions. J. Appl. Physiol. 99, 1138–1148.

Hunt, J., Wray, A., Moin, P., Eddies, streams, and convergence zones in turbulent flows. In Studying Turbulence Using Numerical Simulation Databases, 2 Proceedings of the 1988 Summer Program, pp. 193-208.

Javaheri, S., Wexler, L., 2005. Prevalence and treatment of breathing disorders during sleep in patients with heart failure. Current Treat. Opt. Cardiovascular Med. 7, 295–306.

Kavcic, P., Koren, A., Koritnik, B., Dolenc Groselj, L., 2013. Sleep apnea and snoring. Neurology 81, 691.

Li, C., Jiang, J., Dong, H., Zhao, K., 2017. Computational modeling and validation of human nasal airflow under various breathing conditions. J. Biomech. 64, 59–68.

Lin, C.-L., Tawhai, M.H., McLennan, G., Hoffman, E.A., 2007. Characteristics of the turbulent laryngeal jet and its effect on airflow in the human intra-thoracic airways. Respir. Physiol. Neurobiol. 157, 295–309.

Liu, G., Ren, Y., Dong, H., Akanyeti, O., Liao, J.C., Lauder, G.V., 2017. Computational analysis of vortex dynamics and performance enhancement due to body-fin and fin-fin interactions in fish-like locomotion. J. Fluid Mech. 829, 65–88.

Liu, H., Prot, V.E., Skallerud, B.H., 2018a. 3D patient-specific numerical modeling of the soft palate considering adhesion from the tongue. J. Biomech. 77, 107–114.

Liu, H., Prot, V.E., Skallerud, B.H., 2019. Soft palate muscle activation: a modeling approach for improved understanding of obstructive sleep apnea. Biomech. Model. Mechanobiol. 18, 531–546.

Liu, Y., Mitchell, J., Chen, Y., Yim, W., Chu, W., Wang, R.C., 2018b. Study of the upper airway of obstructive sleep apnea patient using fluid structure interaction. Respir. Physiol. Neurobiol. 249, 54–61.

Liu, Z.S., Luo, X.Y., Lee, H.P., Lu, C., 2007. Snoring source identification and snoring noise prediction. J. Biomech. 40, 861–870.

Madani, M., 1999. Radio frequency somnoplasty: a new treatment for snoring and sleep apnea. Int. J. Oral Maxillofac. Surg. 28, 108–109.

Mihaescu, M., Mylavarapu, G., Gutmark, E.J., Powell, N.B., 2011. Large Eddy Simulation of the pharyngeal airflow associated with Obstructive Sleep Apnea Syndrome at pre and post-surgical treatment. J. Biomech. 44, 2221–2228.

Mittal, R., Dong, H., Bozkurttas, M., Najjar, F., Vargas, A., von Loebbecke, A., 2008. A versatile sharp interface immersed boundary method for incompressible flows with complex boundaries. J. Comput. Phys. 227, 4825–4852.

Miyazaki, S., Itasaka, Y., Ishikawa, K., Togawa, K., 1998. Acoustic analysis of snoring and the site of airway obstruction in sleep related respiratory disorders. Acta Otolaryngol. 118, 47–51.

Mylavarapu, G., Murugappan, S., Mihaescu, M., Kalra, M., Khosla, S., Gutmark, E., 2009. Validation of computational fluid dynamics methodology used for human upper airway flow simulations. J. Biomech. 42, 1553–1559.

Patil, S.P., Schneider, H., Schwartz, A.R., Smith, P.L., 2007. Adult Obstructive sleep apnea: pathophysiology and diagnosis. Chest 132, 325–337.
Pirnar, J., Dolenc-Grošelj, L., Fajdiga, I., Žun, I., 2015. Computational fluid-structure interaction simulation of airflow in the human upper airway. J. Biomech. 48, 3685–3691.
Powell, N.B., Mihaescu, M., Mylavarapu, G., Weaver, E.M., Guilleminault, C., Gutmark, E., 2011. Patterns in pharyngeal airflow associated with sleep-disordered breathing. Sleep Med. 12, 966–974.
Srinivasan, V.R., Low, C., Goodyear, P.W.A., Derbyshire, S., Veetil, A., 2008. Evaluation of Somnoplasty using Snoring Symptom Inventory. Otolaryngol. Head Neck Surg. 139, P82.
Stuck, B.A., Leitzbach, S., Maurer, J.T., 2012. Effects of continuous positive airway pressure on apnea-hypopnea index in obstructive sleep apnea based on long-term compliance. Sleep Breath 16, 467–471.
Sun, X., Yu, C., Wang, Y., Liu, Y., 2007. Numerical simulation of soft palate movement and airflow in human upper airway by fluid-structure interaction method. Acta Mech. Sin. 23, 359–367.
Varghese, S.S., Frankel, S.H., Fischer, P.F., 2007. Direct numerical simulation of stenotic flows. Part 1. Steady flow. J. Fluid Mech. 582, 253–280.
Wang, J., Han, P., Sanchez, Y., Xi, J., Dong, H., 2018. Computational Analysis on Aerodynamics and Vortex Formation of Sleep Apnea, ASME 2018 5th Joint US-European Fluids Engineering Division Summer Meeting. American Society of Mechanical Engineers, pp. V001T002A003-V001T002A003.
Wang, J., Ren, Y., Li, C., Dong, H., 2019. Computational investigation of wing-body interaction and its lift enhancement effect in hummingbird forward flight. Bioinspirat. Biomimetics 14, 046010.
Wang, Y., Elghobashi, S., 2014. On locating the obstruction in the upper airway via numerical simulation. Respir. Physiol. Neurobiol. 193, 1–10.
Wang, Y., Wang, J., Liu, Y., Yu, S., Sun, X., Li, S., Shen, S., Zhao, W., 2012. Fluid–structure interaction modeling of upper airways before and after nasal surgery for obstructive sleep apnea. Int. J. Numerical Meth. Biomed. Eng. 28, 528–546.
Xi, J., April Si, X., Dong, H., Zhong, H., 2018a. Effects of glottis motion on airflow and energy expenditure in a human upper airway model. Eur. J. Mech. B. Fluids 72, 23–37.
Xi, J., Longest, P.W., 2008. Numerical predictions of submicrometer aerosol deposition in the nasal cavity using a novel drift flux approach. Int. J. Heat Mass Transf. 51, 5562–5577.
Xi, J., Si, X., Kim, J., Su, G., Dong, H., 2014. Modeling the pharyngeal anatomical effects on breathing resistance and aerodynamically generated sound. Med. Biol. Eng. Comput. 52, 567–577.
Xi, J., Wang, Z., Talaat, K., Glide-Hurst, C., Dong, H., 2018b. Numerical study of dynamic glottis and tidal breathing on respiratory sounds in a human upper airway model. Sleep Breathing 22, 463–479.
Young, T., Palta, M., Dempsey, J., Skatrud, J., Weber, S., Badr, S., 1993. The occurrence of sleep-disordered breathing among middle-aged adults. N. Engl. J. Med. 328, 1230–1235.
Zhang, Z., Kleinstreuer, C., 2011. Laminar-to-turbulent fluid–nanoparticle dynamics simulations: Model comparisons and nanoparticle-deposition applications. Int. J. Numerical Meth. Biomed. Eng. 27, 1930–1950.
Zhao, M., Barber, T., Cistulli, P.A., Sutherland, K., Rosengarten, G., 2013. Simulation of upper airway occlusion without and with mandibular advancement in obstructive sleep apnea using fluid-structure interaction. J. Biomech. 46, 2586–2592.
Zhu, J.H., Lee, H.P., Lim, K.M., Lee, S.J., Teo, L.S.L., Wang, D.Y., 2012. Passive movement of human soft palate during respiration: A simulation of 3D fluid/structure interaction. J. Biomech. 45, 1992–2000.